European Journal of Medicinal Chemistry 262 (2023) 115862

Contents lists available at ScienceDirect

European Journal of Medicinal Chemistry

journal homepage: www.elsevier.com/locate/ejmech

Research paper

Next generation fibroblast activation protein (FAP) targeting PET tracers - The tetrazine ligation allows an easy and convenient way to ^{18}F-labeled (4-quinolinoyl)glycyl-2-cyanopyrrolidines

Christian B.M. Poulie [a,b,1], Vladimir Shalgunov [a,b,1], Filipe Elvas [c], Yentl Van Rymenant [d], Euy-Sung Moon [e], Umberto Maria Battisti [a,b], Joni De Loose [d], Ingrid De Meester [d], Frank Rösch [e], Pieter Van Der Veken [d], Matthias M. Herth [a,b,f,*]

[a] Department of Drug Design and Pharmacology, Faculty of Health and Medical Sciences, University of Copenhagen, Jagtvej 160, 2100, Copenhagen, Denmark
[b] TetraKit Technologies, Ole Maaløes Vej 3, 2200, Copenhagen, Denmark
[c] Molecular Imaging and Radiology (MIRA), Faculty of Medicine and Health Sciences, University of Antwerp, Universiteitsplein 1, 2610, Wilrijk, Belgium
[d] Laboratory of Medical Biochemistry, Department of Pharmaceutical Sciences, University of Antwerp, 2610, Wilrijk, Belgium
[e] Department of Chemistry, Johannes Gutenberg University, 55131, Mainz, Germany
[f] Department of Clinical Physiology, Nuclear Medicine & PET, Copenhagen University Hospital, Rigshospitalet, Blegdamsvej 9, 2100, Copenhagen, Denmark

ARTICLE INFO

Keywords:
Tetrazine ligation
FAPI
Fluorine-18
Theranostics
PET

ABSTRACT

Small-molecular fibroblast activation protein inhibitor (FAPI)-based tracer have been shown to be promising Positron Emission Tomography (PET) ^{68}Ga-labeled radiopharmaceuticals to image a variety of tumors including pancreatic, breast, and colorectal cancers, among others. In this study, we developed a novel ^{18}F-labeled FAPI derivative. [^{18}F]**6** was labeled using a synthon approach based on the tetrazine ligation. It showed subnanomolar affinity for the FAP protein and a good selectivity profile against known off-target proteases. Small animal PET studies revealed high tumor uptake and good target-to-background ratios. [^{18}F]**6** was excreted via the liver. Overall, [^{18}F]**6** showed promising characteristics to be used as a PET tracer and could serve as a lead for further development of halogen-based theranostic FAPI radiopharmaceuticals.

1. Introduction

Fibroblast activation protein (FAP) is a serine protease which has been described to cleave peptides such as neuropeptide Y, substance P or human fibroblast growth factor 21 in the human body. It belongs to the dipeptidyl peptidase (DPP) protein family [1]. Under physiological conditions, FAP is typically not expressed in healthy tissues, benign lesions or precancerous tissues [2,3]. In contrast, FAP is highly overexpressed in the stroma of most of epithelial-derived tumors in the context of Cancer Associated Fibroblasts (CAF) and is consistently expressed in both bone and soft-tissue tumors, including pancreatic, breast, and colorectal cancers, among others (Fig. 1A) [4,5]. This characteristic makes it an ideal pan-tumor target for Positron Emission Tomography (PET). PET is a non-invasive imaging technique that allows for patient stratification, disease monitoring or therapy planning, for example [6–8].

Recently, FAPI tracers have attracted a lot of interest within the field. Especially, tracers based on the highly potent and selective (4-quinolinoyl)glycyl-2-cyanopyrrolidine derivative (UAMC1110) appear to be highly suitable to image FAP in vivo (Fig. 1A). This motif is not only of high binding affinity to FAP, it is also extremely selective over other DPPs [9] – a challenge for many other small molecules targeting FAP [10]. Due to the attractiveness of CAF as oncological target, several ^{68}Ga-labeled FAPI PET tracers including [^{68}Ga]Ga-FAPI-04 (Fig. 1B), [11], Al[^{18}F]F-NOTA-FAPI-04, [12], [^{68}Ga]Ga-FAPI-46 [13], [^{18}F]F-FAPI-73, [14], Al[^{18}F]F-FAPI-74, [14,15], [^{68}Ga]Ga-DOTA.SA.FAPI or [^{68}Ga]Ga-DATA^{5m}.SA.FAPI have been developed and successfully translated to systematic application in patients [16–18].

In this study, we set out to develop an ^{18}F-labeled FAPI derivative that could (i) benefit from the various advantages of fluorine-18 instead

* Corresponding author. Department of Drug Design and Pharmacology, Faculty of Health and Medical Sciences, University of Copenhagen, Jagtvej 160, 2100, Copenhagen, Denmark.
E-mail address: matthias.herth@sund.ku.dk (M.M. Herth).
[1] These authors contributed equally.

https://doi.org/10.1016/j.ejmech.2023.115862
Received 30 June 2023; Received in revised form 5 October 2023; Accepted 6 October 2023
Available online 14 October 2023

of gallium-68, and (ii) which could easily be translated into a therapeutic agent based on either iodine-131 (^{131}I) or astatine-211 (^{211}At). Fluorine-18 is the most clinically applied radionuclide for PET imaging due to its almost ideal decay properties such as its half-life of approximately 110 min, its high β^+-branching ratio of 96 % and its low β^+-energy of 635 keV. These characteristics result for example in the possibility to produce activity amounts which are sufficient for several scans or to distribute the corresponding radiopharmaceutical to other radiopharmacies or hospitals [19,20]. Additionally, ^{18}F-labeled tracers result in a relatively low radiation burden of typically around 15 mSv [21,22] and in high spatial resolution images (0.54 FWHM, image resolutions in the low mm range are possible using modern clinical scanners) [23]. Beside these beneficial imaging qualities, covalent labeling with fluorine-18 also allows easy replacement of fluorine with other halogens such as ^{131}I and ^{211}At. Iodine-131 is a β^--emitter that is widely used for radionuclide therapy and is accessible in almost unlimited quantities. Astatine-211 is an α-emitter that is considered – by many scientists – to be the best emitter for targeted alpha-radionuclide therapy (TAT) [24–26]. TAT has been shown to eradicate cancer metastases that could not be eradicated with β^--emitters [27].

In order to develop such a theranostic approach, we based our labeling strategy on the tetrazine ligation [28,29]. The tetrazine ligation is a two-step reaction between a constrained *trans*-cyclooctene (TCO) and a 1,2,4,5-tetrazine (Tz). The reaction is initiated via an inverse-electron-demand Diels–Alder (IEDDA) reaction, followed by a spontaneous retro-Diels-Alder reaction, with the expulsion of nitrogen gas. As such, the tetrazine ligation results in a covalent bonding between the two reaction partners. The reaction can be carried out in aqueous solution, at room temperature and with low precursor amounts (ca. 10–50 μg), making any HPLC purification obsolete. Due to its ultra-fast second order-rate constants, the tetrazine ligation can be carried out quantitatively within 5–10 min [28,29]. The one downside of this ligation is the formation of several region and tautomeric click products (Fig. 1C). Regardless, this approach has been successfully employed in the synthesis of various peptide-based tracers, such as [^{18}F]RGD, [30], [^{18}F]interleukin-2 [31] as well as [^{18}F]octreotide derivatives [32]. Recently we have demonstrated the successful labelling of such polar Tzs, either with fluorine-18, as well as iodine-125 [33–40]. Fig. 1D displays the strategy of our development approach. In here, we aim to extend this approach to FAPI-based tracers, by incorporation of polar tetrazines, which should increase kidney excretion.

2. Results and discussion

2.1. Chemistry

2.1.1. Design

Due to its excellent selectivity over other dipeptidyl peptidases and prolyl oligopeptidase, UAMC1110 was selected as the FAP binding motif. A C4-aliphatic chain and a squaramide-bridged C6-aliphatic chain were selected as the linkers and are based on previous successful FAPI tracers [16,18]. To these structures, we linked a TCO-carbamate resulting in our precursor moieties. The Tz was selected from a H-Tz containing a polar moiety (2,2'-(benzylazanediyl)diacetic acid). This Tz was selected because of its superior second order-rate constants and we selected this polar group to promote solubility and potentially increase kidney excretion. The calculated LogD ($cLogD_{7.4}$) values for compounds **4**–**7** are;-2.67, -2.60, -3.49 and -3.42, respectively. In addition to the polar moiety, the selected Tz was designed to bear either a fluorine or an iodine substituent on the phenyl ring.

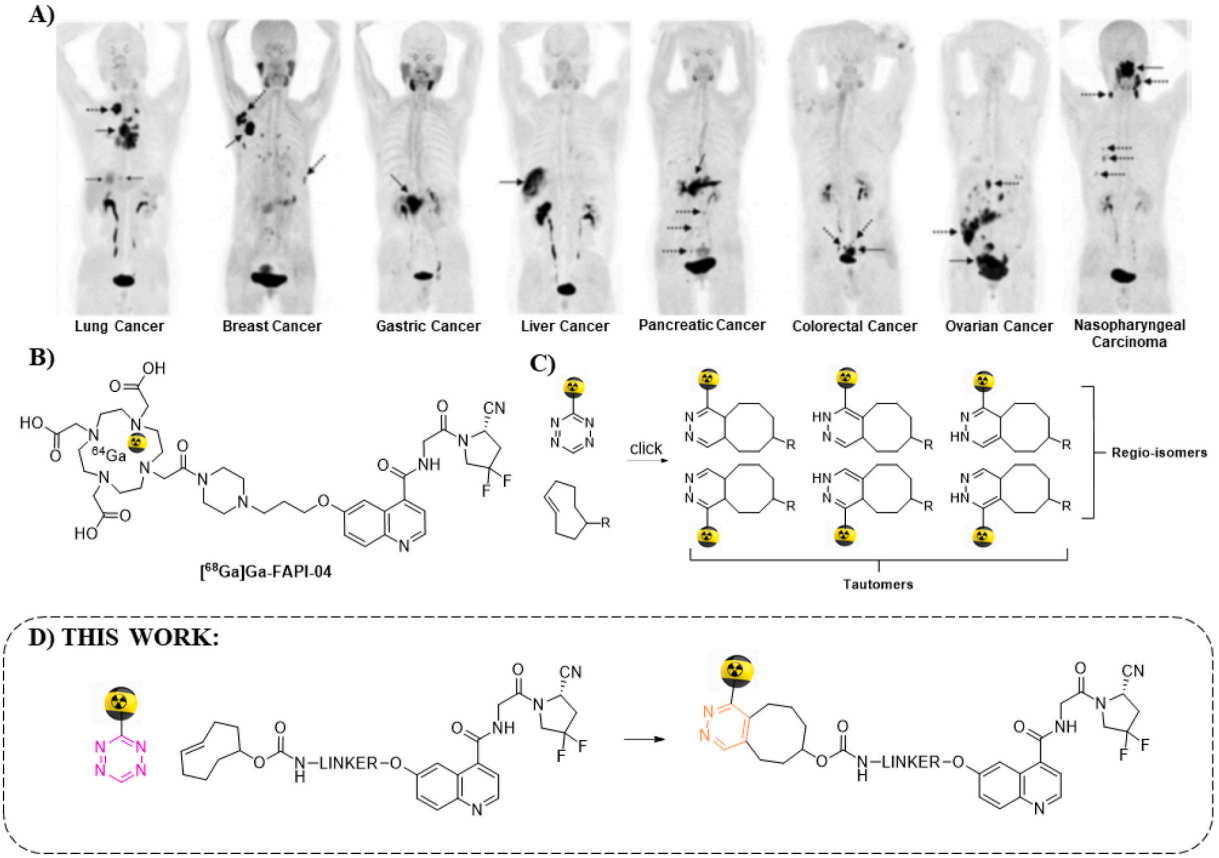

Fig. 1. (A) PET images of [^{68}Ga]Ga-FAPI-04 in various types of cancers. Data adopted with permission from Ref. [41]; (B) Chemical structure of [^{68}Ga]Ga-FAPI-04; (C) Overview of the different region and tautometic products resulting from the Tz ligation; (D) Overview of the strategy employed within this study.

2.1.2. Synthesis

Synthesis of **1** was performed according to a previously reported procedure [42]. Subsequently, **1** was reacted with equatorial TCO-PNB-ester [43–46] in DMF, in the presence of Et_3N, which yielded TCO-FAPI **2** in 34 % isolated yield (Scheme 1). The synthesis of TCO-FAPI **3** commenced for the common intermediate **1**. The installation of the squaramide was performed according to a reported procedure [16] and the installation of the TCO-carbamate was performed analogously to TCO-FAPI **2**, which resulted in 38 % isolated yield (Scheme 1). Both the F- and the I-Tz, as well as the stannyl precursor for radiolabeling, were prepared according to previously reported procedures [36,39,40]. The synthesis of **4**–**5** and **6**–**7** was achieved by mixing the corresponding Tz with **2** or **3**, respectively, in equimolar ratios (Scheme 1). The ligation proceeded instantly, and the subsequent auto-oxidation was achieved by letting the reaction mixtures stir in an open vial, for three days. After full oxidation, from the dihydropyridazines to the corresponding pyridazines, the compounds were purified by semi-preparative HPLC, which yielded in a 60–85 % yield. Products were isolated as their corresponding TFA salts (Scheme 1).

2.2. Pharmacological characterization

2.2.1. In vitro evaluation

IC_{50} values for all developed structures (**4**–**5**, **6**–**7**) were determined for FAP, PREP and DPP4, 8 and 9 and compared to the reference inhibitor UAMC1110 [47,48]. For FAP, all four analogues exhibited subnanomolar IC_{50} values, with the two squaramide containing analogues (**6**–**7**), being slightly more affine (Table 1). None of the compounds had any appreciable affinity for PREP (selectivity index >1000-fold) (Table 1). Interestingly, there is a strong difference in the affinity for DPP4: compounds **4**–**5** display IC_{50} values of >1 μM, while compounds **6**–**7** have significantly lower IC_{50} values (380 and 290 nM, respectively) (Table 1). However, due to the high potency towards FAP, the selectivity indices for FAP/DPP4 are still well within an acceptable range (>650 and > 450-fold, respectively) (Table 1). The compounds in this study have a slightly higher affinity for DPP8 and 9 when compared to the closely related DOTA.SA.FAPI (Table 1) [16] However, especially compound 6 with selectivity indices of >200 towards the related intracellular DPP8 and 9, is expected to image selectively FAP when applied in vivo. Additionally, the selectivity over DPP8 and 9 is less of a concern, as these enzymes are expressed intracellularly.

Table 1
IC_{50} values of compounds **4**–**7** for FAP and the different related serine proteases (DPP4, DPP8, DPP9 and PREP).[a]

Compound	FAP IC_{50} (nM)	PREP IC_{50} (nM)	DPP4 IC_{50} (nM)	DPP8 IC_{50} (nM)	DPP9 IC_{50} (nM)
4	0.85 ± 0.09	2100 ± 200 (2471)	2410 ± 140 (2835)	160 ± 10 (188)	360 ± 60 (424)
5	0.94 ± 0.04	1100 ± 100 (1170)	1440 ± 230 (1532)	50 ± 10 (53)	220 ± 20 (234)
6	0.56 ± 0.03	2400 ± 300 (4285)	380 ± 30 (679)	120 ± 10 (214)	140 ± 20 (250)
7	0.60 ± 0.02	1500 ± 20 (2500)	290 ± 10 (483)	110 ± 10 (183)	170 ± 10 (283)
UAMC1110	0.43 ± 0.02[a]	1800 ± 10[a] (4186)	>10,000[b] (>20,000)	>10,000[b] (>20,000)	7790 ± 830[b] (18,116)

[a] All data are presented in nM ± the mean with standard deviation (n = 3 for FAP, PREP and DPP8 and DPP4, n = 2 for DPP9). Data in brackets are the corresponding selectivity indices towards FAP (a) data from ref [48].
[b] data from ref [47].

2.3. Radiosynthesis

2.3.1. Radiolabeling of [^{18}F]6

Compound [^{18}F]**6** was obtained by reacting the radioactive tetrazine [^{18}F]**11** with the TCO **3**. [^{18}F]**11** was prepared by copper-mediated ^{18}F-fluorodestannylation as described by García-Vázquez et al. [38,40]. TCO **3** (0.83 mg/mL in MeOH) was added in 2:1 M excess to a solution of tetrazine [^{18}F]**11** with a molar activity of 10.41 ± 0.85 GBq/μmol, followed by reaction at room temperature. After 10 min, full conversion of [^{18}F]**11** to [^{18}F]**6** was observed by radio-HPLC (Scheme 2).

2.4. Pharmacological characterization (in vivo/ex vivo evaluation)

2.4.1. PET and ex vivo biodistribution investigations

Due to the more favorable selectivity indices for the squaramide derivatives and being the more polar analogue, [^{18}F]**6** was selected for in vivo μPET studies. We evaluated its tumor uptake in two xenograft models, HT-29 and U87MG. [^{18}F]**6** was administered via the tail vein, and the biodistribution imaged over a time span of 60 min (Fig. 2). Afterwards, the animals were euthanized, tissues were dissected, and the

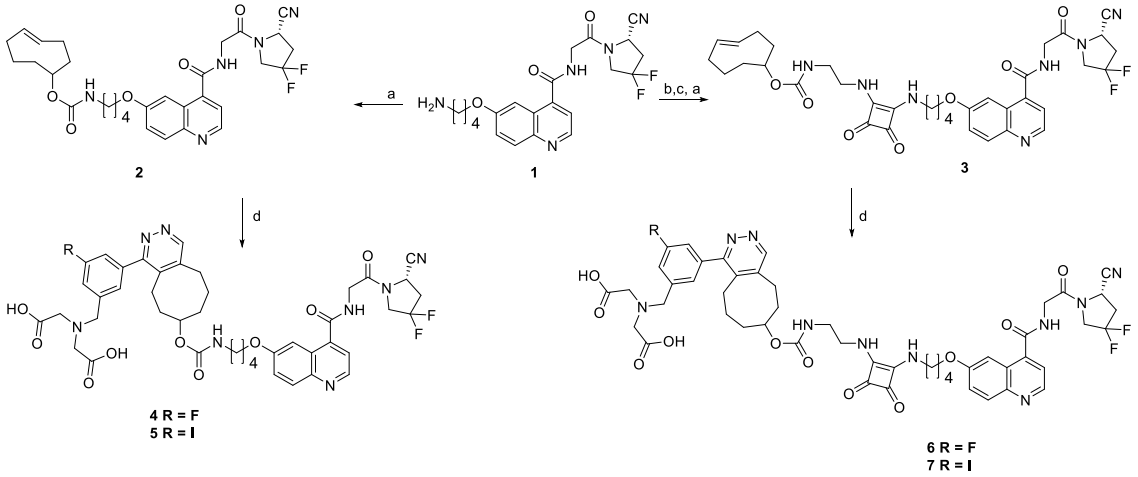

Scheme 1. Chemical synthesis of halogenated FAPi tracers (only one regioisomeric form depicted); (a) TCO-PNB, Et_3N, DMF, RT, dark, overnight, (34–38 %); (b) 3,4-diethoxycyclobut-3-ene-1,2-dione, Na_2HPO_4/NaH_2PO_4 buffer (pH 7), RT, overnight (67 %); (c) ethane-1,2-diamine, Na_2HPO_4 buffer (pH 9), RT, overnight (78 %); (d) Corresponding tetrazine, $MeCN/H_2O$, open vial, RT, 3 days (60–85 %).

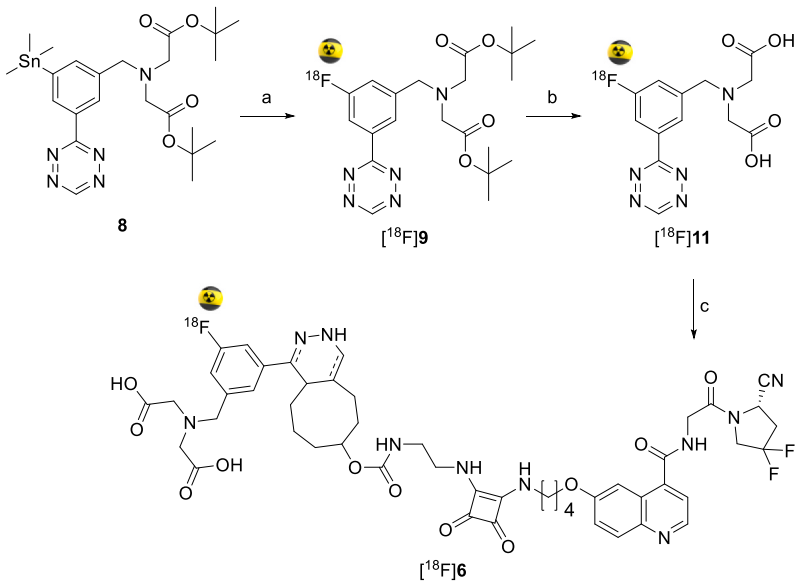

Scheme 2. Synthesis of [^{18}F]**6** (only one tautomeric and regioisomeric form depicted); (a) Cu(OTf)$_2$ pyridine, [^{18}F]KF, DMA, 100 °C, 5 min; (b) TFA, 80 °C, 10 min (5.34% RCY (over two steps); (c) **3**, RT, EtOH/buffer (Quant).

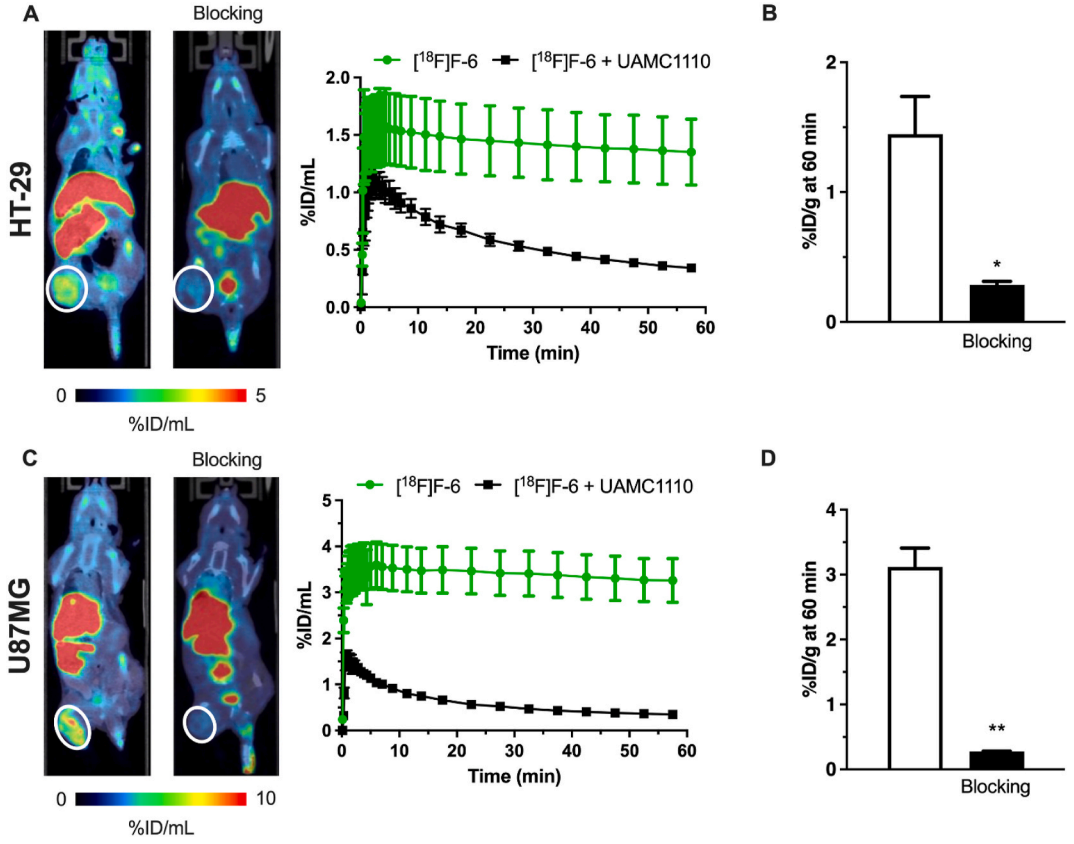

Fig. 2. In vivo μPET imaging analysis and ex vivo tumor uptake of [^{18}F]**6**. (A) in HT-29 and (C) U87MG xenografts. Representative coronal small-animal PET/CT images (average 30–60 min) and time-activity curves of HT-29 and U87MG tumor–bearing animals using [^{18}F]**6**. Tumor indicated with white circle (B and D) respective blocking experiments with competitor UAMC1110 (5 mg/kg). Data are expressed as mean ± SEM * p = 0.0277, **p = 0.0023, unpaired 2-tailed Student *t*-test.

amount of radioactivity was determined. The tumors were clearly visible in the μPET images. The background uptake was low in both tumor models. A clear blocking effect of UAMC1110 was observed, indicating that [^{18}F]**6** indeed bound to the FAP protein (Fig. 2). The accumulation in the tumor at 60 min post injection (p.i.) in the HT-29 model and the U87MG model was 1.35 ± 0.57 (n = 4) and 3.26 ± 0.95 % ID/mL (n = 4), respectively (Fig. 2). μPET images of both xenograft models displayed significant uptake in the liver and small intestines of [^{18}F]**6**

(Fig. 2). This uptake was unexpected as [^{18}F]**6** is highly polar (cLogD$_{7.4}$ = −3.49). Consequently, renal excretion was expected. Ex vivo studies verified the in vivo biodistribution pattern. Uptake in other non-specific organs and tissues was relatively low. In the U87MG model, also update in the bones was observed, which was blocked by co-administration of UAMC1110. Interestingly, the bone uptake was increased when UAMC1110 was administered in the HT-29 model. In this model, also the stomach uptake was increased when [^{18}F]**6** was co-administrated with UAMC1110 (Fig. 3).

2.4.2. *Ex vivo and histologic analysis of FAP expression in the tumors*

Autoradiography (ARG) and immunohistochemistry (IHC) analysis were performed in both tumor models. ARG of HT-29 and U87MG tumor sections showed a high accumulation of [^{18}F]**6** in both tumors and co-localization of increased radioactivity uptake within areas of increased FAP expression, as demonstrated by the increased levels of FAP immunoreactivity (Fig. 4A). In the blocking groups, low accumulation of [^{18}F]**6** was observed in the autoradiographs, despite high levels of FAP expression confirming the specificity of [^{18}F]**6** for FAP.

To determine how well the radiotracer uptake reproduces FAP expression in the tumors, quantitative FAP staining was performed on whole tumor sections. The radiotracer uptake was in good agreement with FAP immunoreactivity in the tumors. In accordance with the higher radiotracer uptake, U87MG xenografts showed higher FAP expression when compared to HT-29 xenografts. Notably, [^{18}F]**6** showed a good correlation between whole tumor mean radioactivity and FAP expression in histologic sections (Fig. 4B). Different FAP expression profiles were observed in HT-29 and U87MG xenograft models. In the HT-29 tumors, FAP expression was restricted to the tumor stroma whereas in the U87MG tumors FAP was expressed in both tumor and glioblastoma cancer cells themselves (Fig. 4A).

3. Conclusions

In this project, we designed new ^{18}F-labeled FAPI derivatives for PET imaging by covalently linking halogen containing Tz synthons with two different FAPI-TCO precursors. These two precursors differ in the linker region, one consists of a C4-aliphatic chain and the other a squaramide-bridged C6-aliphatic chain. All four compounds displayed sub-nanomolar affinity for the FAP protein. However, in respect to well established off-targets, the squaramide containing structures outperformed the C4-aliphatic chain linked tracers, especially with respect for selectivity over DPP8. For this reason, [^{18}F]**6** was selected for in vivo μPET evaluation in two different tumor models (HT-29 and U87MG). [^{18}F]**6** showed good tumor uptake. High uptake in the liver and small intestines was also observed. Uptake in other non-specific organs and tissues was low. With respect to imaging, [^{18}F]**6** displayed an excellent biodistribution profile. However, further optimization is needed to translate this tracer into a ^{131}I- or ^{211}At-labeled derivative. The detected uptake in the liver of [^{18}F]**6** for such applications is most likely too high for therapeutic applications. Nonetheless, compound [^{18}F]**6** showed promising results and is an excellent lead compound for further development of halogen based theranostic FAPI tracers.

4. Methods

4.1. *Chemistry*

All reactions involving dry solvents or sensitive agents were performed under an argon atmosphere and glassware was dried prior to use. Commercially available chemicals were used without further purification. Solvents were dried prior to use with an SG water solvent purification system or dried by standard procedures. Automated Flash Column Chromatography was performed on a CombiFlash NextGen 300+ system supplied by TeleDyne ISCO, equipped with RediSep silica packed columns. Detection of the compounds was carried out by means of a UV–Vis variable wavelength detector operating from 200 to 800 nm and by Evaporative Light Scattering Detector (ELSD). Solvent systems for separation were particular for each compound but consisted of various mixtures of heptane, EtOAc, DCM and MeOH. ^{1}H NMR spectra were recorded on a 600 MHz Bruker Avance III HD, and ^{13}C NMR spectra on a 151 MHz Bruker Avance III HD. Preparative HPLC was carried out on an Ultimate Thermo SCIENTIFIC HPLC system with an LPG-3200BX pump, a Rheodyne 9721i injector, a 10 mL loop, an MWD-3000SD detector (200, 210, 225 and 254 nm), and a Gemini-NX C18 (250 × 21.2 mm, 5 μm) column for preparative purifications. Solvent A: H_2O + 0.1 % TFA; Solvent B: MeCN–H_2O 9:1 + 0.1 % TFA. For HPLC control, data collection and data handling, Chromeleon software v. 6.80 was used. UPLC-MS spectra were recorded using an Acquity UPLC H-Class Waters series solvent delivery system equipped with an autoinjector coupled to

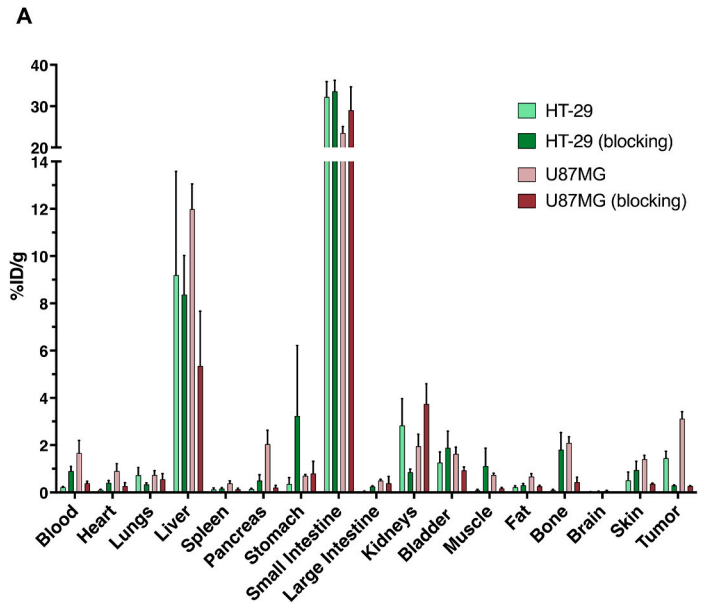

B

	HT-29	U87MG
Blood	6.50	1.87
Lungs	1.99	4.25
Liver	0.16	0.26
Spleen	11.89	8.18
Pancreas	10.46	1.53
Small Intestine	0.04	0.13
Large Intestine	28.91	6.25
Kidneys	0.51	1.60
Muscle	15.96	4.26

Fig. 3. A) Ex vivo biodistribution of [^{18}F]**6** in HT-29 and U87MG xenografts at 60 min p. i., without (control) and with co-administration of UAMC-1110 (blocking, 5 mg/kg, n = 4). **B**) Tumor-to-organ ratios of 'background' organs.

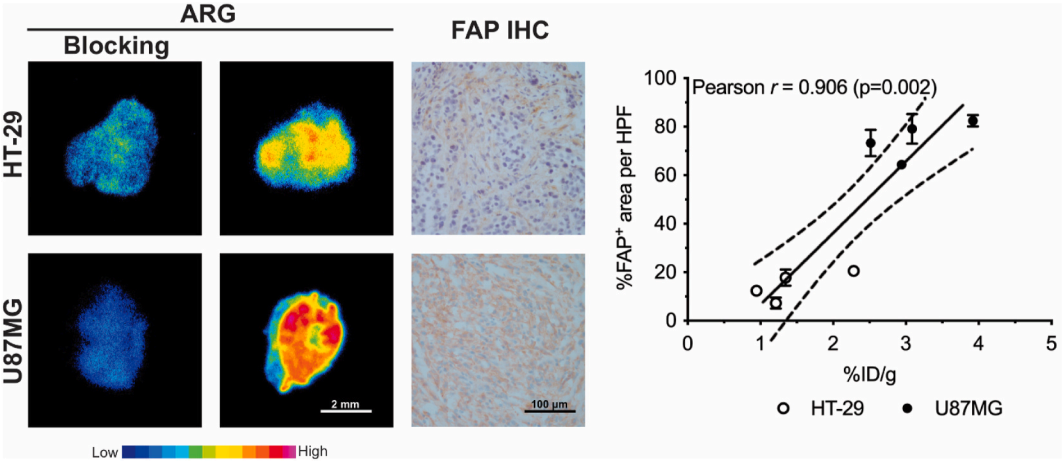

Fig. 4. Ex vivo evaluation of radiotracer uptake and FAP expression in HT-29 and U87MG tumors. (A) Representative autoradiography (ARG) and microscopy images of adjacent tumor sections from mice injected with [^{18}F]**6**. (B) Quantitative and correlation analysis of levels of FAP-positive cells to radiotracer uptake in the tumors. Pearson correlation (r) and two-tailed *p* values are shown in the top left corner of chart.

an Acquity QDa and TUV detectors installed with an Acquity UPLC®BEH C18 (50 × 2.1 mm, 1.7 µm) column. Solvent A: 5 % aq MeCN +0.1 % HCO_2H: Solvent B: MeCN +0.1 % HCO_2H. Usually, gradients from A:B 1:0 to 1:1 (5 min) or A:B 1:0 to 0–50 (5 min), were performed depending on the polarity of the compounds. For data collection and data handling, MassLynx software was used. Compounds were dried under high vacuum or lyophilized using a ScanVac Cool Safe Freeze Drier. All tested compounds are >95 % pure, by HPLC analysis.

4.2. (S)-6-(4-aminobutoxy)-N-(2-(2-cyano-4,4-difluoropyrrolidin-1-yl)-2-oxoethyl)quinoline-4-carboxamide (1)

Was prepared according to previously reported procedure [42].

4.3. (E)-Cyclooct-4-en-1-yl (4-((4-((2-((S)-2-cyano-4,4-difluoropyrrolidin-1-yl)-2-oxoethyl)carbamoyl)quinolin-6-yl)oxy)butyl) carbamate (2)

Et_3N (27 µL, 0.19 mmol, 1.6 eq) was added to a solution of **1** (50 mg, 0.12 mmol, 1 eq) in dry DMF (600 µL), to which was added TCO-PNB ester (34 mg, 0.12 mmol, 1 eq) and the reaction was stirred at room temperature for 24 h in the dark. After completion the DMF was removed azeotropically, with the addition of heptane and the crude mixture was submitted to semi-preparative HPLC purification. The fractions containing product were lyophilized, which yielded 32 mg of a white solid (34 %, 0.04 mmol). MS (ESI) m/z = 584.3 $[M + H]^+$; ^{1}H NMR (600 MHz, DMSO) δ 9.09 (t, J = 6.0 Hz, 1H), 8.82 (dd, J = 102.3, 4.4 Hz, 1H), 7.98 (d, J = 9.2 Hz, 1H), 7.90–7.82 (m, 1H), 7.52 (d, J = 4.4 Hz, 1H), 7.46 (dd, J = 9.2, 2.7 Hz, 1H), 6.98 (t, J = 5.9 Hz, 1H), 6.74 (s, 1H), 5.57 (ddd, J = 15.3, 10.9, 4.0 Hz, 1H), 5.43 (ddd, J = 15.7, 11.1, 3.5 Hz, 1H), 5.15 (d, J = 8.2 Hz, 1H), 4.33 (ddd, J = 15.8, 11.2, 4.4 Hz, 1H), 4.24 (t, J = 6.4 Hz, 2H), 4.22–4.19 (m, 1H), 4.13 (t, J = 6.6 Hz, 2H), 3.08–2.99 (m, 2H), 2.96–2.91 (m, 3H), 2.87–2.74 (m, 1H), 2.31–2.23 (m, 2H), 1.93–1.87 (m, 2H), 1.86–1.80 (m, 1H), 1.80–1.74 (m, 2H), 1.68–1.61 (m, 1H), 1.61–1.55 (m, 3H), 1.55–1.50 (m, 1H). ^{13}C NMR (151 MHz, DMSO) δ 168.0, 167.4, 158.0, 157.8, 157.1, 155.8, 155.6, 147.2, 134.89, 132.5, 130.4, 125.5, 122.8, 119.2, 117.7, 104.5, 78.9, 77.6, 67.8, 44.2, 44.2, 41.3, 40.7, 38.2, 33.7, 32.1, 30.6, 28.2, 26.1, 25.9.

4.4. (E)-Cyclooct-4-en-1-yl (2-((2-((4-((4-((2-((S)-2-cyano-4,4-difluoropyrrolidin-1-yl)-2-oxoethyl)carbamoyl)quinolin-6-yl)oxy)butyl) amino)-3,4-dioxocyclobut-1-en-1-yl)amino)ethyl)carbamate (3)

3,4-diethoxycyclobut-3-ene-1,2-dione (47 mg, 0.278 mmol, 1.2 eq) was dissolved in 0.5 M Na_2HPO_4/NaH_2PO_4 phosphate buffer (1 mL, pH 7), to which was added **1** (100 mg, 0.231 mmol, 1 eq) and stirred at room temperature for 18 h. The crude mixture was submitted to semi-preparative HPLC purification (67 %). The lyophilized fractions (86 mg, 0.155 mmol, 1 eq) were dissolved in 0.5 M Na_2HPO_4 phosphate buffer (500 µL, pH 9), to which was added ethane-1,2-diamine (103 µL, 1.549 mmol, 10 eq). The crude mixture was submitted to semi-preparative HPLC purification (78 %). The lyophilized fraction (66 mg, 0.116, 1 eq) were dissolved in dry DMF (800 µL), to which was added Et_3N (48 µL, 0.346 mmol, 3 eq) and TCO-PNB ester (34 mg, 0.116 mmol, 1 eq) and the reaction was stirred at room temperature for 24 h, in the dark. After completion the DMF was removed azeotropically, with the addition of heptane and the crude mixture was submitted to semi-preparative HPLC purification. The fractions containing product were lyophilized, which yielded 32 mg of a white solid (38 %, 0.04 mmol). MS (ESI) m/z = 722.3 $[M + H]^+$; ^{1}H NMR (400 MHz, DMSO) δ 11.03 (bs, 2H), 9.08 (t, J = 6.0 Hz, 1H), 8.83 (d, J = 4.4 Hz, 1H), 7.99 (d, J = 9.2 Hz, 1H), 7.89 (d, J = 2.8 Hz, 1H), 7.53 (d, J = 4.4 Hz, 1H), 7.47 (dd, J = 9.2, 2.7 Hz, 1H), 7.06–7.01 (m, 1H), 5.54 (ddd, J = 14.8, 10.1, 4.0 Hz, 1H), 5.46–5.35 (m, 1H), 5.14 (dd, J = 9.4, 2.8 Hz, 1H), 4.41–4.28 (m, 2H), 4.24 (d, J = 6.0 Hz, 2H), 4.18 (t, J = 6.4 Hz, 3H), 3.54 (d, J = 38.4 Hz, 4H), 3.20–3.04 (m, 3H), 3.01–2.89 (m, 1H), 2.89–2.76 (m, 1H), 2.28–2.18 (m, 2H), 1.95–1.78 (m, 6H), 1.78–1.68 (m, 2H), 1.68–1.42 (m, 3H).

4.5. 6-(4-((((4-(3-((Bis(carboxymethyl)amino)methyl)-5-fluorophenyl)-5,6,7,8,9,10-hexahydrocycloocta[d]pyridazin-7-yl)oxy) carbonyl)amino)butoxy)-4-((2-((S)-2-cyano-4,4-difluoropyrrolidin-1-yl)-2-oxoethyl)carbamoyl)quinolin-1-ium 2,2,2-trifluoroacetate (4)

To a solution of **2** (4.00 mg, 5.7 µmol, 1 eq) in MeCN (500 µL) was added 2,2'-((3-fluoro-5-(1,2,4,5-tetrazin-3-yl)benzyl)azanediyl)diacetic acid (2.46 mg, 5.7 µmol, 1 eq). After 5 min, the pink solution has turned colourless. At this point, H_2O (500 µL) was added and the reaction was stirred for 3 d at room temperature, in an open vial. After complete oxidation, the crude mixture was submitted to semi-preparative HPLC purification. The fractions containing product were lyophilized, which yielded 4.0 mg of an off-white solid (80 %, 4.6 µmol). MS (ESI) m/z = 875.4 $[M + H]^+$; MS (ESI) m/z = 438.3 $[M + 2H]^{2+}$. ^{1}H NMR (600 MHz,

MeOD) (as a mixture of diastereoisomers and regioisomers) δ 9.01 (d, J = 30.7 Hz, 1H), 8.78 (d, J = 4.7 Hz, 1H), 7.99 (d, J = 9.2 Hz, 1H), 7.96 (d, J = 2.7 Hz, 1H), 7.63 (d, J = 4.6 Hz, 1H), 7.50 (dd, J = 9.2, 2.7 Hz, 1H), 7.40 (t, J = 11.9 Hz, 2H), 7.24 (dd, J = 15.8, 8.6 Hz, 1H), 5.20–5.07 (m, 1H), 4.58–4.40 (m, 1H), 4.37–4.28 (m, 2H), 4.28–4.19 (m, 4H), 4.17–4.10 (m, 3H), 3.66 (s, 3H), 3.18–3.14 (m, 2H), 3.11–3.03 (m, 1H), 2.99–2.72 (m, 6H), 2.00–1.93 (m, 1H), 1.92–1.79 (m, 4H), 1.77–1.58 (m, 6H).

4.6. 6-(4-((((4-(3-((Bis(carboxymethyl)amino)methyl)-5-iodophenyl)-5,6,7,8,9,10-hexahydrocycloocta[d]pyridazin-7-yl)oxy)carbonyl)amino) butoxy)-4-((2-((S)-2-cyano-4,4-difluoropyrrolidin-1-yl)-2-oxoethyl) carbamoyl)quinolin-1-ium 2,2,2-trifluoroacetate (5)

To a solution of **2** (4.00 mg, 5.7 μmol, 1 eq) in MeCN (500 μL) was added 2,2'-((3-iodo-5-(1,2,4,5-tetrazin-3-yl)benzyl)azanediyl)diacetic acid (1.84 mg, 5.7 μmol, 1 eq). After 5 min, the pink solution has turned colourless. At this point, H_2O (500 μL) was added and the reaction was stirred for 3 d at room temperature, in an open vial. After complete oxidation, the crude mixture was submitted to semi-preparative HPLC purification. The fractions containing product were lyophilized, which yielded 4.8 mg of an off-white solid (85 %, 4.9 μmol). MS (ESI) m/z = 983.3 $[M + H]^+$; MS (ESI) m/z = 492.2 $[M + 2H]^{2+}$. ^{1}H NMR (600 MHz, MeOD) (as a mixture of diastereoisomers and regioisomers) δ 9.01 (d, J = 30.5 Hz, 1H), 8.79 (d, J = 4.7 Hz, 1H), 8.04–7.94 (m, 3H), 7.83 (d, J = 15.8 Hz, 1H), 7.63 (d, J = 4.6 Hz, 1H), 7.58 (d, J = 12.2 Hz, 1H), 7.50 (dd, J = 9.2, 2.6 Hz, 1H), 5.20–5.07 (m, 1H), 4.54–4.39 (m, 1H), 4.39–4.29 (m, 2H), 4.29–4.19 (m, 3H), 4.19–4.04 (m, 3H), 3.67 (s, 3H), 3.22–3.14 (m, 2H), 3.11–3.01 (m, 1H), 3.00–2.85 (m, 3H), 2.86–2.69 (m, 3H), 2.15–2.08 (m, 1H), 2.00–1.93 (m, 1H), 1.92–1.78 (m, 4H), 1.77–1.55 (m, 6H).

4.7. 6-(4-((2-((2-((((1-(3-((Bis(carboxymethyl)amino)methyl)-5-fluorophenyl)-5,6,7,8,9,10-hexahydrocycloocta[d]pyridazin-7-yl)oxy) carbonyl)amino)ethyl)amino)-3,4-dioxocyclobut-1-en-1-yl)amino) butoxy)-4-((2-((S)-2-cyano-4,4-difluoropyrrolidin-1-yl)-2-oxoethyl) carbamoyl)quinolin-1-ium 2,2,2-trifluoroacetate (6)

To a solution of **3** (4.00 mg, 4.8 μmol, 1 eq) in MeCN (500 μL) was added 2,2'-((3-fluoro-5-(1,2,4,5-tetrazin-3-yl)benzyl)azanediyl)diacetic acid (1.54 mg, 4.8 μmol, 1 eq). After 5 min, the pink solution has turned colourless. At this point, H_2O (500 μL) was added and the reaction was stirred for 3 d at room temperature, in an open vial. After complete oxidation, the crude mixture was submitted to semi-preparative HPLC purification. The fractions containing product were lyophilized, which yielded 2.9 mg of an off-white solid (60 %, 2.9 μmol). MS (ESI) m/z = 1013.4 $[M + H]^+$; ^{1}H NMR (600 MHz, MeOD) (as a mixture of diastereoisomers and regioisomers) δ 8.99 (d, J = 30.9 Hz, 1H), 8.81 (dd, J = 4.7, 1.2 Hz, 1H), 8.01 (d, J = 8.9 Hz, 1H), 7.94 (d, J = 2.4 Hz, 1H), 7.64 (d, J = 4.7 Hz, 1H), 7.56 (d, J = 9.1 Hz, 1H), 7.41 (t, J = 10.1 Hz, 2H), 7.28 (dd, J = 16.7, 8.4 Hz, 1H), 5.21–5.10 (m, 1H), 4.61–4.48 (m, 1H), 4.41–4.30 (m, 5H), 4.27–4.11 (m, 4H), 3.97–3.82 (m, 1H), 3.80–3.77 (m, 1H), 3.74 (s, 2H), 3.70–3.59 (m, 4H), 3.31–3.24 (m, 1H), 3.15–2.99 (m, 1H), 3.00–2.83 (m, 3H), 2.83–2.64 (m, 3H), 2.00–1.91 (m, 4H), 1.90–1.80 (m, 3H), 1.79–1.58 (m, 4H).

4.8. 6-(4-((2-((2-((((1-(3-((Bis(carboxymethyl)amino)methyl)-5-iodophenyl)-5,6,7,8,9,10-hexahydrocycloocta[d]pyridazin-7-yl)oxy) carbonyl)amino)ethyl)amino)-3,4-dioxocyclobut-1-en-1-yl)amino) butoxy)-4-((2-((S)-2-cyano-4,4-difluoropyrrolidin-1-yl)-2-oxoethyl) carbamoyl)quinolin-1-ium 2,2,2-trifluoroacetate (7)

To a solution of **3** (10.00 mg, 12 μmol, 1 eq) in MeCN (1 mL) was added 2,2'-((3-iodo-5-(1,2,4,5-tetrazin-3-yl)benzyl)azanediyl)diacetic acid (5.14 mg, 12 μmol, 1 eq). After 5 min, the pink solution has turned colourless. At this point, H_2O (1 mL) was added and the reaction was stirred for 3 d at room temperature, in an open vial. After complete oxidation, the crude mixture was submitted to semi-preparative HPLC purification. The fractions containing product were lyophilized, which yielded 9.4 mg of an off-white solid (70 %, 8.4 μmol). MS (ESI) m/z = 1121.4 $[M + H]^+$; ^{1}H NMR (600 MHz, MeOD) (as a mixture of diastereoisomers and regioisomers) δ 8.99 (d, J = 31.0 Hz, 1H), 8.83 (dd, J = 4.7, 1.2 Hz, 1H), 8.09–8.06 (m, 1H), 8.05–8.00 (m, 2H), 7.88–7.81 (m, 1H), k7.69 (dd, J = 4.7, 2.2 Hz, 1H), 7.60 (d, J = 29.1 Hz, 1H), 7.54 (td, J = 9.6, 2.8 Hz, 1H), 5.13 (dd, J = 9.6, 2.9 Hz, 1H), 4.62–4.45 (m, 1H), 4.39–4.27 (m, 5H), 4.27–4.09 (m, 4H), 3.99–3.83 (m, 1H), 3.79–3.76 (m, 1H), 3.75 (s, 2H), 3.70–3.57 (m, 4H), 3.28–3.22 (m, 1H), 3.17–2.99 (m, 1H), 3.00–2.85 (m, 3H), 2.85–2.69 (m, 3H), 2.01–1.90 (m, 4H), 1.89–1.79 (m, 3H), 1.79–1.57 (m, 4H).

4.9. 2,2'-((3-(1,2,4,5-tetrazin-3-yl)-5-(trimethylstannyl)benzyl) azanediyl)diacetic acid (8)

Was prepared according to previously reported procedure [39,40].

4.10. Lipophilicity determinations

The $cLogD_{7.4}$ of compounds **4**–**7** were calculated using the Chemaxon Chemicalize software.

4.11. Radiochemistry

No-carrier-added aqueous [^{18}F]fluoride was produced in an Eclipse HP cyclotron (Siemens) using the $^{18}O(p,n)^{18}F$ reaction by proton bombardment of [^{18}O]H_2O (Rotem Industries).

The radiosynthesis of [^{18}F]**11** was based on earlier work by García-Vázquez et al. [38,40] and performed on the Trasis AllInOne synthesizer (Belgium) with a custom-built cassette. Approximately 19.06 GBq of [^{18}F]fluoride was trapped on a QMA cartridge (preconditioned with 5 mL 90 mg/mL KOTf and 5 mL ultrapure water) and then eluted into a reaction vessel with a solution of 50 μg K_2CO_3 and 10 mg KOTf in 0.6 mL ultrapure water. After azeotropic drying at 100 °C with two additions of acetonitrile, the radiolabeling solution was added to the reactor. This freshly-prepared solution consisted of 3–4 mg trimethylstannane precursor **8** and 7.2 mg $Cu(OTf)_2$ and 12 μL pyridine, dissolved in 600 μL DMA solvent. The mixture was heated at 100C for 5 min, after which the reaction was quenched with H_2O, containing 0.1 % TFA, and passed through a C18 Short SPE cartridge (Waters) pre-wetted with 50 % ethanol. The cartridge was rinsed with water and eluted with MeCN (2 mL). To the eluate was added 37 % HCl (1 mL), the mixture was heated for 5 min at 60 °C, further diluted with 0.6 M phosphate buffer (pH 12) and injected on HPLC. Semipreparative HPLC purification (Luna C18(2) column, 10 × 250 mm, 5 μm; mobile phase EtOH/water- 15/85 v/v, 4 mL/min) afforded a purified [^{18}F]**11** (retention time 10.8 min) in a radiochemical yield of 5.34 ± 2.82% (decay-corrected to end-of-bombardment) and radiochemical purity >95 %. The molar activity (MA) of [^{18}F]**11** was 10.41 ± 0.85 GBq/μmol (n = 4).

Compound [^{18}F]**6** was obtained by addition of a 2:1 M excess of **3** in MeOH (0.83 mg/mL) to a solution of HPLC-purified [^{18}F]**11**, followed by 10 min reaction at room temperature. [^{18}F]**6** was fully consumed during the click reaction, therefore no purification of [^{18}F]**11** was needed.

Conversion of [^{18}F]**11** to [^{18}F]**6** was followed by radio-HPLC. Quality control was performed using analytical radio-HPLC and a Shimadzu LC-20AT HPLC equipped with an SPD-20A UV/VIS detector (λ = 250 nm) in series with a NaI-scintillation detector for radiation detection (Raytest). HPLC column and method: Phenomenex Luna C18(2) 150 × 4.6 mm (5 μm) HPLC column. Gradient method: 0–1 min – 15 % MeCN, 8–9 min – 85 % MeCN, 9.5–10 min – 15 % MeCN (+0.1 % TFA) in water (+0.1%TFA), with a flow rate of 1.5 mL/min. The recorded data were processed by the GINA-Star 5 software (Raytest).

4.12. Pharmacology

4.12.1. Enzymes

Recombinant human FAP (rhFAP, extracellular domain, amino acid 27–760) with a C-terminal His-tag was expressed and purified in Sf9 insect cells and purified from the supernatant as described before [18]. Human DPP4 was purified from human seminal plasma. Recombinant human PREP was expressed in BL21(DE3) cells and purified as by De Decker et al. [49] Recombinant human DPP8 and DPP9 were expressed using an N-terminal His-tag and were purified as described [49].

4.12.2. IC_{50} measurements

IC_{50} values for all enzymes were determined using the protocol described in Van Rymenant et al. [47] Fluorogenic substrates were used since the compounds interfered with the colorimetric measuremet of the routinely used *p*-nitroaniline derived substrates [47]. Briefly, IC_{50} measurements for FAP were performed using *Z*-Gly-Pro-7-amino-4-methylcoumarine (AMC) (Bachem) as the substrate at a concentration of 50 μM at pH 8 (0.05 M Tris-HCl buffer, 1 mg/mL BSA and 140 mM NaCl). IC_{50} values for PREP were determined using *N*-succinyl-Gly--Pro-AMC (Bachem) as the substrate at a concentration of 250 μM at pH 7.4 (0.1 M K-phosphate, 1 mM EDTA, 1 mM DTT and 1 mg/mL BSA). H-Gly-Pro-AMC was used as the substrate for the DPPs at the respective final concentrations of 65 μM (DPP4) and 100 μM (DPP8/DPP9) at pH 7.6 (0.1 M Tris-HCl buffer with 0.1 M NaCl and 0.1 mg/mL BSA).

For all IC_{50} measurements, the compounds were pre-incubated with the respective enzyme for 15 min at 37 °C, afterwards the substrate was added and the velocities of AMC release were measured kinetically $\lambda_{ex} =$ 380 nm, $\lambda_{em} = 465$ nm for at least 15 min at 37 °C. Measurements were performed on the Infinite 200 (Tecan Group Ltd.) and the Magellan software was used to process the data. Data were analyzed and fitted using GraFit 7 software using a non-linear fit model. In each assay, at least eight concentrations of compound were tested. Furthermore, the final solvent DMSO concentration was kept constant during the experiment to exclude any solvent effects.

4.12.3. Data analysis

The data were fitted using a non-linear fit model in GraFit 7, according to the following equation:

$$y = \frac{range}{1 + \left(\frac{x}{IC_{50}}\right)^{s}}$$

where y is the value of the residual enzymatic activity compared to a non-inhibited sample, x is the final inhibitor concentration in the assay, s is the slope factor and the IC_{50} is the half maximal inhibitory concentration.

4.12.4. In vivo animal studies and ex vivo biodistribution

All the experimental procedures involving animals were approved by the local ethics committee (2021–01, University of Antwerp, Belgium). Six-to eight-week-old female CD1$^{-/-}$ nude mice (body weight, 20–25 g; Charles River Laboratories) were inoculated by subcutaneous injection into the hind flank with HT29 (10×10^6, n = 8; ATCC HTB-38) or U87MG (5×10^6, n = 8; ATCC HTB-14) tumor cells, both in 100 μL of Dulbecco phosphate-buffered saline. When tumor volumes reached approximately 200 mm^3, mice underwent PET/CT scanning.

4.12.5. For in vivo

PET/CT (Inveon, Siemens), tumor-bearing CD1$^{-/-}$ nude mice (n = 16) were anesthetized using isoflurane (5 % for induction, 2 % for maintenance), placed on the animal bed in the scanner and injected via lateral tail vein catheterization with 3.7–8.5 MBq of [^{18}F]-**6**. To confirm the binding specificity of each radiotracer, a cohort of tumor-bearing mice (n = 8) was injected via the tail vein with UAMC1110 30 min before radiotracer injection. Throughout the entire PET/CT scanning procedure, the mice were maintained at constant body temperature by using a heating pad.

4.12.6. Dynamic whole-body

PET images were acquired during 60 min (12×10s, 3×20s, 3×30s, 3×60s, 3×150s and 9×300s frames). Following each PET acquisition, a whole-body CT scan was acquired to obtain anatomic information for segmentation. For quantitative analysis, PET data were reconstructed using a list-mode iterative reconstruction with proprietary spatially variant resolution modeling in 8 iterations and 16 subsets of the 3D ordered subset expectation maximization (OSEM 3D) algorithm [50]. The PET images were additionally reconstructed on a $128 \times 128 \times 159$ matrix with a voxel size of $0.776 \times 0.776 \times 0.776$ mm. CT-based attenuation and single scatter stimulation (SSS) scatter corrections were applied to the PET data. Volumes of interest (VOIs) were manually drawn on the PET/CT images using PMOD (version 3.6; PMOD Technologies) to delineate the tumor regions. The average tumor activity per volume was obtained from the co-registered PET images and the decay-corrected time-activity curves (TACs) were extracted. For an absolute measure of tracer uptake, normalized images were scaled according to the percent injected dose (%ID mL^{-1} = tissue uptake [kBq mL^{-1}]/injected dose [kBq] × 100). After the scans, the organs and tissues were harvested, weighed and the radioactivity in the samples was measured using an automatic γ-counter. The uptake levels of the tracers in the organs and tissues were expressed as percentage of the injected dose per gram (%ID g^{-1}).

4.12.7. Autoradiography and immunohistochemistry analysis

After γ-counting, the tumors were immediately snap-frozen, embedded in OCT compound (VWR), sectioned (100 μm), and exposed to phosphor screen plates (Fujifilm) overnight. Exposed plates were imaged in a Phosphor Imager system (FLA7000; GE Healthcare) for visualization of regional tracer distribution in the tumors.

Adjacent tumor sections (10 μm) were taken at regular intervals across the entire tumor volume and used for immunohistochemical analysis of FAP expression in the tumor xenografts. The slides were post fixed with 4 % paraformaldehyde, rinsed with PBS (phosphate-buffered saline), followed by a blocking step using PBS with 3 % horse serum and 0.1 % Triton-X. The slides were subsequently washed with PBS, followed by incubation with a primary anti-FAP antibody (R&D, AF3715, 1:100) in blocking buffer overnight at room temperature. The next day, the slides were washed with PBS and incubated with anti-sheep secondary antibody (1:2000), for 1 h at room temperature, followed by DAB staining (DAKO). The nuclei were counterstained using Mayer's hematoxylin (Merck). Light microscopic images were grabbed using an CX31 upright microscope (Olympus) coupled with a Nikon DS-Vi1 color camera. Quantification of FAP expression was performed in 14–16 randomly selected high power magnification (×400) images collected across three non-sequential tumor sections (n = 8 tumors) using IHC profiler plug-in for ImageJ v1.53, as previously described [51]. The tumor areas were annotated manually based on the nuclear counterstain. FAP expression was calculated as the mean percentage of positive stained area per high-power field per tumor and correlated to the corresponding ex vivo radiotracer uptake in the tumor.

4.12.8. Statistical analysis

Experimental data were expressed as mean ± standard deviation (SD). All statistical analysis were performed using Prism (version 9.5.1; GraphPad Software). Statistical significance between two data sets was evaluated by the unpaired two-tailed Student *t*-test. For correlation analysis, the Pearson correlation coefficient was computed. Differences between the groups were considered statistically significant if the *P* value of was less than 0.05.

Author contributions

Conceptualization: MMH, FR, PVDV; Manuscript preparation: CBMP, VS; Organic Chemistry: CBMP, E-SM, UMB; Radiochemistry: VS; In vitro pharmacology: YVR, JDL, IDM; In vivo pharmacology: FE.

Notes

The authors declare the following competing financial interest(s): Poulie, Shalgunov, Battisti, and Herth are co-founders of TetraKit Technologies.

Declaration of competing interest

The authors declare the following financial interests/personal relationships which may be considered as potential competing interests: Matthias M. herth reports a relationship with Tetrakit Technologies that includes: board membership, consulting or advisory, and equity or stocks. Christian B. M. Poulie reports a relationship with Tetrakit Technologies that includes: board membership, employment, and equity or stocks. Vladimir Shalgunov reports a relationship with Tetrakit Technologies that includes: board membership, employment, and equity or stocks. Umberto Maria Battisti reports a relationship with Tetrakit technologies that includes: board membership, employment, and equity or stocks.

Data availability

Data will be made available on request.

Acknowledgements

The authors thank the Danish Research Council for Independent Research (grant agreement no. 8022-00358B) for financial support. Yentl Van Rymenant was supported by the FWO-SB fellowship (1S64222 N) and Joni De Loose was supported by FWO-FR fellowship (11B3322 N).

Appendix A. Supplementary data

Supplementary data related to this article can be found at https://doi.org/10.1016/j.ejmech.2023.115862.

References

[1] L. Juillerat-Jeanneret, P. Tafelmeyer, D. Golshayan, Fibroblast activation protein-α in fibrogenic disorders and cancer: more than a prolyl-specific peptidase? Expert Opin. Ther. Targets 21 (10) (2017) 977–991.
[2] M.J. Scanlan, B.K. Raj, B. Calvo, P. Garin-Chesa, M.P. Sanz-Moncasi, J.H. Healey, L. J. Old, W.J. Rettig, Molecular cloning of fibroblast activation protein alpha, a member of the serine protease family selectively expressed in stromal fibroblasts of epithelial cancers, Proc. Natl. Acad. Sci. USA 91 (12) (1994) 5657–5661.
[3] O. Dohi, H. Ohtani, M. Hatori, E. Sato, M. Hosaka, H. Nagura, E. Itoi, S. Kokubun, Histogenesis-specific expression of fibroblast activation protein and dipeptidylpeptidase-IV in human bone and soft tissue tumours, Histopathology 55 (4) (2009) 432–440.
[4] J. Calais, FAP: the next billion dollar nuclear theranostics target? J. Nucl. Med. 61 (2) (2020) 163–165.
[5] E. Puré, R. Blomberg, Pro-tumorigenic roles of fibroblast activation protein in cancer: back to the basics, Oncogene 37 (32) (2018) 4343–4357.
[6] F. Giammarile, P. Castellucci, R. Dierckx, E. Estrada Lobato, M. Farsad, R. Hustinx, A. Jalilian, O. Pellet, S. Rossi, D. Paez, Non-FDG PET/CT in Diagnostic Oncology: A Pict. Rev. Eur. J. Hybrid Imaging 3 (1) (2019) 20.
[7] J.L. Kristensen, M.M. Herth, Textbook of Drug Design and Discovery: in Vivo Imaging in Drug Discovery. In Textbook of Drug Design and Discovery (Fifth Edition), CRC Press, 2017.
[8] M. Piel, I. Vernaleken, F. Rösch, Positron emission Tomography in CNS drug discovery and drug monitoring, J. Med. Chem. 57 (22) (2014) 9232–9258.
[9] F.M. Keane, N.A. Nadvi, T.-W. Yao, M.D. Gorrell, Y. Neuropeptide, B-type natriuretic peptide, substance P and peptide YY are novel substrates of fibroblast activation protein-α, FEBS J. 278 (8) (2011) 1316–1332.
[10] K. Jansen, H. De Winter, L. Heirbaut, J.D. Cheng, J. Joossens, A.-M. Lambeir, I. De Meester, K. Augustyns, P. Van der Veken, Selective inhibitors of fibroblast activation protein (FAP) with a xanthine scaffold, Med. Chem. Commun. 5 (11) (2014) 1700–1707.
[11] T. Lindner, A. Loktev, A. Altmann, F. Giesel, C. Kratochwil, J. Debus, D. Jäger, W. Mier, U. Haberkorn, Development of quinoline-based theranostic ligands for the targeting of fibroblast activation protein, J. Nucl. Med. 59 (9) (2018) 1415–1422.
[12] X. Jiang, X. Wang, T. Shen, Y. Yao, M. Chen, Z. Li, X. Li, J. Shen, Y. Kou, S. Chen, et al., FAPI-04 PET/CT using [18F]AlF labeling strategy: automatic synthesis, quality control, and in vivo assessment in patient, Front. Oncol. 11 (2021).
[13] A. Loktev, T. Lindner, E.-M. Burger, A. Altmann, F. Giesel, C. Kratochwil, J. Debus, F. Marmé, D. Jäger, W. Mier, et al., Development of fibroblast activation protein–targeted radiotracers with improved tumor retention, J. Nucl. Med. 60 (10) (2019) 1421–1429.
[14] T. Lindner, A. Altmann, F. Giesel, C. Kratochwil, C. Kleist, S. Krämer, W. Mier, J. Cardinale, H.-U. Kauczor, D. Jäger, et al., 18F-Labeled tracers targeting fibroblast activation protein, EJNMMI Rad. Chem. 6 (1) (2021) 26.
[15] F.L. Giesel, S. Adeberg, M. Syed, T. Lindner, L.D. Jiménez-Franco, E. Mavriopoulou, F. Staudinger, E. Tonndorf-Martini, S. Regnery, S. Rieken, et al., FAPI-74 PET/CT using either 18 F-AlF or cold-kit 68 Ga labeling: biodistribution, radiation dosimetry, and tumor delineation in lung cancer patients, J. Nucl. Med. 62 (2) (2021) 201–207.
[16] E.S. Moon, Y. Van Rymenant, S. Battan, J. De Loose, A. Bracke, P. Van der Veken, I. De Meester, F. Rösch, In Vitro evaluation of the squaramide-conjugated fibroblast activation protein inhibitor-based agents AAZTA5.SA.FAPi and DOTA.SA.FAPi, Molecules 26 (12) (2021) 3482.
[17] S. Ballal, M.P. Yadav, E.S. Moon, V.S. Kramer, F. Roesch, S. Kumari, C. Bal, First-in-human results on the biodistribution, pharmacokinetics, and dosimetry of [177Lu] Lu-DOTA.SA.FAPi and [177Lu]Lu-dotaga. (SA.FAPi)2, Pharmaceuticals 14 (12) (2021) 1212.
[18] E.S. Moon, F. Elvas, G. Vliegen, S. De Lombaerde, C. Vangestel, S. De Bruycker, A. Bracke, E. Eppard, L. Greifenstein, B. Klasen, et al., Targeting fibroblast activation protein (FAP): next generation PET radiotracers using squaramide coupled bifunctional DOTA and DATA5m chelators, EJNMMI Rad. Chem. 5 (1) (2020) 19.
[19] J. Ducharme, A.L. Goertzen, J. Patterson, S. Demeter, Practical aspects of 18F-FDG PET when receiving 18F-FDG from a distant supplier, J. Nucl. Med. Technol. 37 (3) (2009) 164–169.
[20] K. Bratteby, C.L. Denholt, S. Lehel, I.N. Petersen, J. Madsen, M. Erlandsson, T. Ohlsson, M.M. Herth, N. Gillings, Fully automated GMP-compliant synthesis of [18F]FE-PE2I, Pharmaceuticals 14 (7) (2021) 601.
[21] A. Kaushik, A. Jaimini, M. Tripathi, M. D'Souza, R. Sharma, A. Mondal, A. Mishra, B. Dwarakanath, Estimation of radiation dose to patients from [18] FDG whole body PET/CT investigations using dynamic PET scan protocol, Indian J. Med. Res. 142 (6) (2015) 721.
[22] H.W. Kwon, J.P. Kim, H.J. Lee, J.C. Paeng, J.S. Lee, G.J. Cheon, D.S. Lee, J.-K. Chung, K.W. Kang, Radiation dose from whole-body F-18 fluorodeoxyglucose Positron emission tomography/computed Tomography: nationwide survey in Korea, J. Kor. Med. Sci. 31 (Suppl 1) (2016) S69.
[23] W.W. Moses, Fundamental limits of spatial resolution in PET, Nucl. Instrum. Methods Phys. Res. Sect. A Accel. Spectrom. Detect. Assoc. Equip. 648 (2011) S236–S240.
[24] F. Li, Y. Yang, J. Liao, N. Liu, Recent progress of astatine-211 in endoradiotherapy: great advances from fundamental properties to targeted radiopharmaceuticals, Chin. Chem. Lett. 33 (7) (2022) 3325–3338.
[25] P. Albertsson, T. Bäck, K. Bergmark, A. Hallqvist, M. Johansson, E. Aneheim, S. Lindegren, C. Timperanza, K. Smerud, S. Palm, Astatine-211 based radionuclide therapy: current clinical trial landscape, Front. Med. 9 (2023).
[26] R. Zimmerman, Alpha emitters from an industrial perspective, 12th International Symposium on Targeted Alpha Therapy (TAT 12) (2023).
[27] C. Kratochwil, F. Bruchertseifer, F.L. Giesel, M. Weis, F.A. Verburg, F. Mottaghy, K. Kopka, C. Apostolidis, U. Haberkorn, A. Morgenstern, 225 Ac-PSMA-617 for PSMA-targeted α-radiation therapy of metastatic castration-resistant prostate cancer, J. Nucl. Med. 57 (12) (2016) 1941–1944.
[28] M. Staudt, M. Herth, M.; B.M. Poulie, C. Pretargeted theranostics. In theranostics - an old concept in new clothing, Intech (2021).
[29] E.J.L. Stéen, P.E. Edem, K. Nørregaard, J.T. Jørgensen, V. Shalgunov, A. Kjaer, M. M. Herth, Pretargeting in nuclear imaging and radionuclide therapy: improving efficacy of theranostics and nanomedicines, Biomaterials 179 (2018) 209–245.
[30] R. Selvaraj, S. Liu, M. Hassink, C. Huang, L. Yap, R. Park, J.M. Fox, Z. Li, P.S. Conti, Tetrazine-trans-cyclooctene ligation for the rapid construction of integrin Avβ3 targeted PET tracer based on a cyclic RGD peptide, Bioorg. Med. Chem. Lett. 21 (17) (2011) 5011–5014.
[31] L. Allott, A. Amgheib, C. Barnes, M. Braga, D. Brickute, N. Wang, R. Fu, S. Ghaem-Maghami, E.O. Aboagye, Radiolabelling an 18 F biologic via facile IEDDA "click" Chemistry on the GE FASTLab™ platform, React. Chem. Eng. 6 (6) (2021) 1070–1078.
[32] S. Otaru, A. Paulus, S. Imlimthan, I. Kuurne, H. Virtanen, H. Liljenbäck, T. Tolvanen, T. Auchynnikava, A. Roivainen, K. Helariutta, et al., Development of [18 F]AmBF 3 tetrazine for radiolabeling of peptides: preclinical evaluation and PET imaging of [18 F]AmBF 3 -PEG 7 -tyr 3 -octreotide in an AR42J pancreatic carcinoma model, Bioconjugate Chem. 33 (7) (2022) 1393–1404.
[33] R. García-Vázquez, J.T. Jørgensen, K.E. Bratteby, V. Shalgunov, L. Hvass, M. M. Herth, A. Kjær, U.M. Battisti, Development of 18F-labeled bispyridyl tetrazines for in vivo pretargeted PET imaging, Pharmaceuticals 15 (2) (2022) 245.

[34] U.M. Battisti, R. García-Vázquez, D. Svatunek, B. Herrmann, A. Löffler, H. Mikula, M.M. Herth, Synergistic experimental and computational investigation of the bioorthogonal reactivity of substituted aryltetrazines, Bioconjugate Chem. 33 (4) (2022) 608–624.
[35] E.J.L. Stéen, J.T. Jørgensen, C. Denk, U.M. Battisti, K. Nørregaard, P.E. Edem, K. Bratteby, V. Shalgunov, M. Wilkovitsch, D. Svatunek, et al., Lipophilicity and click reactivity determine the performance of bioorthogonal tetrazine tools in pretargeted in vivo Chemistry, ACS Pharmacol. Transl. Sci. 4 (2) (2021) 824–833.
[36] U.M. Battisti, K. Bratteby, J.T. Jørgensen, L. Hvass, V. Shalgunov, H. Mikula, A. Kjær, M.M. Herth, Development of the first aliphatic 18 F-labeled tetrazine suitable for pretargeted PET imaging—expanding the bioorthogonal tool box, J. Med. Chem. 64 (20) (2021) 15297–15312.
[37] R. García-Vázquez, U.M. Battisti, V. Shalgunov, G. Schäfer, M. Barz, M.M. Herth, [11 C]carboxylated tetrazines for facile labeling of trans-cyclooctene-functionalized PeptoBrushes, Macromol. Rapid Commun. 43 (12) (2022) 2100655.
[38] I.V. Andersen, R. García-Vázquez, U.M. Battisti, M.M. Herth, Optimization of direct aromatic 18F-labeling of tetrazines, Molecules 27 (13) (2022) 4022.
[39] N. Bidesi, V. Shalgunov, U.M. Battisti, L. Hvass, J.T. Jørgensen, C.B.M. Poulie, A. I. Jensen, A. Kjaer, M.M. Herth, Synthesis and radiolabeling of a polar [125 I]I-1,2,4,5-tetrazine, J. Label. Compd. Radiopharm. 66 (1) (2023) 22–30.
[40] R. García-Vázquez, U.M. Battisti, J.T. Jørgensen, V. Shalgunov, L. Hvass, D. L. Stares, I.N. Petersen, F. Crestey, A. Löffler, D. Svatunek, et al., Direct Cu-mediated aromatic 18 F-labeling of highly reactive tetrazines for pretargeted bioorthogonal PET imaging, Chem. Sci. 12 (35) (2021) 11668–11675.
[41] L. Zhao, J. Chen, Y. Pang, K. Fu, Q. Shang, H. Wu, L. Sun, Q. Lin, H. Chen, Fibroblast activation protein-based theranostics in cancer Research: a state-of-the-art review, Theranostics 12 (4) (2022) 1557–1569.
[42] M. Martin, S. Ballal, M.P. Yadav, C. Bal, Y. Van Rymenant, J. De Loose, E. Verhulst, I. De Meester, Van der Veken, P.; roesch, F. Novel generation of FAP inhibitor-based homodimers for improved application in radiotheranostics, Cancers 15 (6) (2023) 1889.
[43] P.G. Clark, E.N. Guidry, W.Y. Chan, W.E. Steinmetz, R.H. Grubbs, Synthesis of a molecular charm bracelet via click cyclization and olefin metathesis clipping, J. Am. Chem. Soc. 132 (10) (2010) 3405–3412.
[44] Y. Kurra, K.A. Odoi, Y.-J. Lee, Y. Yang, T. Lu, S.E. Wheeler, J. Torres-Kolbus, A. Deiters, W.R. Liu, Two rapid catalyst-free click reactions for in vivo protein labeling of genetically encoded strained alkene/alkyne functionalities, Bioconjugate Chem. 25 (9) (2014) 1730–1738.
[45] M. Royzen, G.P.A. Yap, J.M. Fox, A photochemical synthesis of functionalized trans -cyclooctenes driven by metal complexation, J. Am. Chem. Soc. 130 (12) (2008) 3760–3761.
[46] C.B.M. Poulie, E. Sporer, L. Hvass, J.T. Jørgensen, P.J. Kempen, S.I. Lopes van den Broek, V. Shalgunov, A. Kjaer, A.I. Jensen, M.M. Herth, Bioorthogonal click of colloidal gold nanoparticles to antibodies In Vivo, Chem. – A Eur. J. 28 (61) (2022).
[47] Y. Van Rymenant, M. Tanc, R. Van Elzen, A. Bracke, O. De Wever, K. Augustyns, A.-M. Lambeir, M. Kockx, I. De Meester, P. Van Der Veken, In vitro and in situ activity-based labeling of fibroblast activation protein with UAMC1110-derived probes, Front. Chem. 9 (2021).
[48] K. Jansen, L. Heirbaut, R. Verkerk, J.D. Cheng, J. Joossens, P. Cos, L. Maes, A.-M. Lambeir, I. De Meester, K. Augustyns, et al., Extended structure–activity relationship and pharmacokinetic investigation of (4-Quinolinoyl)Glycyl-2-cyanopyrrolidine inhibitors of fibroblast activation protein (FAP), J. Med. Chem. 57 (7) (2014) 3053–3074.
[49] A. De Decker, G. Vliegen, D. Van Rompaey, A. Peeraer, A. Bracke, L. Verckist, K. Jansen, R. Geiss-Friedlander, K. Augustyns, H. De Winter, et al., Novel small molecule-derived, highly selective substrates for fibroblast activation protein (FAP), ACS Med. Chem. Lett. 10 (8) (2019) 1173–1179.
[50] A. Miranda, D. Bertoglio, D. Glorie, S. Stroobants, S. Staelens, J. Verhaeghe, Validation of a spatially variant resolution model for small animal brain PET studies, Biomed. Phys. Eng. Express 6 (4) (2020), 045001.
[51] F. Varghese, A.B. Bukhari, R. Malhotra, A. De, IHC profiler: an open source plugin for the quantitative evaluation and automated scoring of immunohistochemistry images of human tissue samples, PLoS One 9 (5) (2014), e96801.